COMMUNICATIONS CHEMISTRY

ARTICLE

DOI: 10.1038/s42004-018-0048-5 OPEN

# Mixed valence salts based on carbon-centered neutral radical crystals

Tsuyoshi Murata[1], Chiaki Yamada[2], Ko Furukawa[3] & Yasushi Morita[1]

Organic neutral radicals have been predicted to exhibit various electronic functions such as electrical conduction. However, most organic neutral radicals are insulators, because they cannot form sufficient intermolecular interactions due to the bulky substituent groups required for stabilization. Here we report that one-dimensional assemblies of carbon-centered neutral π-radicals, namely 4,8,12,trioxotriangulene derivatives, possess effective conducting pathways as a result of strong intermolecular interactions based on two-electron-multicenter bonding. The columns of trioxotriangulene derivatives with weak π-dimerization and uniform π-stacking exhibit semiconducting behaviors, with high conductivities of ~$10^{-3}$ S $cm^{-1}$ as a single component purely organic molecular system. We exploit this general tendency to form one-dimensional assemblies, and the large 25 π-electronic system with a robust condensed polycyclic structure, to obtain mixed-valence salts consisting of neutral radicals and the corresponding anionic species with a higher room-temperature conductivity of 1–125 S $cm^{-1}$.

[1] Department of Applied Chemistry, Faculty of Engineering, Aichi Institute of Technology, Yachigusa 1247, Yakusa, Toyota, Aichi 470-0392, Japan. [2] Department of Chemistry, Graduate School of Science, Osaka University, Machikaneyama 1-1, Toyonaka, Osaka 560-0043, Japan. [3] Centre for Instrumental Analysis, Niigata University, 8050 Ikarashi 2-no-cho, Nishi-ku, Niigata 950-2181, Japan. Correspondence and requests for materials should be addressed to Y.M. (email: moritay@aitech.ac.jp)

Organic conductors have been a focus in the development of molecule-based electronic materials for more than 60 years[1]. Usually, organic compounds are electrical insulators, because the highest occupied molecular orbital (HOMO) band is completely filled and the electron must overcome the large HOMO–LUMO (lowest unoccupied MO) energy gap. The formation of a conduction pathway is also necessary through orbital overlaps between molecules; however, organic molecules are electronically discrete in the solid state. This has been overcome in plural component charge-transfer (CT) complexes and salts, where one-dimensional π-stacking columns with large intermolecular π-orbital overlaps provide a conduction pathway. Semiconducting perylene–bromine salt[2] (room temperature conductivity ($\sigma_{RT}$) ~$10^{-1}$ S cm$^{-1}$) and the first organic metal, TTF–TCNQ complex[3] (tetrathiafulvalene–tetracyanoquinodimethane, $\sigma_{RT}$ = $10^{2}$ S cm$^{-1}$), are classic examples of such systems. In these cases, neutral molecules and radical ionic species of electron-donor and/or electron-acceptor molecules co-exist within a π-stacking column, generating the mixed valence (MV) state. A MV salt forms a partially filled band structure, providing the conduction carrier.

Besides plural component CT complexes and salts, single component neutral π-radicals are also studied for the development of organic conductors[4–6]. The singly occupied MO (SOMO) of a neutral π-radical gives a half-filled band, and the excitation from HOMO to LUMO bands is not necessary. However, most single component neutral π-radicals are insulators or poorly conductive semiconductors ($\sigma_{RT}$ < $10^{-10}$ S cm$^{-1}$) due to the conduction barrier originating from the on-site Coulomb repulsion ($U$, Mott insulator)[7,8] and the steric hindrance needed to impart kinetic stability inhibiting intermolecular interactions[9,10]. High conductivities in single component neutral radicals with $\sigma_{RT}$ > $10^{-6}$ S cm$^{-1}$ have been reported in several systems, such as bisdithiazolyl and related radicals[11–17] ($\sigma_{RT}$ = $4 \times 10^{-2}$ S cm$^{-1}$ at most[17], measured for single crystals), and betainic TCNQ[18] and *N,N'*-dicyanoquinodiiminide[19] radicals ($\sigma_{RT}$ = $3.2 \times 10^{-5}$ and $1.6 \times 10^{-5}$ S cm$^{-1}$ and at most, measured for compressed pellets, respectively), betainic TTF radicals[20] ($\sigma_{RT}$ = $1.0 \times 10^{-1}$ S cm$^{-1}$ at most, measured for compressed pellets), where the heteroatom effects and strong polarizability contribute to the reduction of $U$. It should be noted that carrier doping into neutral radical crystals generates the MV state and dramatically increases conductivity[21,22]. For an example, the conductivity of insulating crystals of 1,4-phenylene-bis(dithiadiazolyl) diradical increased to $\sigma_{RT}$ = 100 S cm$^{-1}$ by doping with iodine as an oxidant[21]. Furthermore, the connection of two TTF units through a π-electronic system effectively reduces $U$, and single component organic metals were realized in zwitterionic TTF dimer dicarboxylate radical[23] ($\sigma_{RT}$ = 530 S cm$^{-1}$, measured for a bulk sheet) and a transition metal complex with two TTF ligands[24] ([Ni(tmdt)$_2$], $\sigma_{RT}$ = 400 S cm$^{-1}$, measured for single crystal). High conductivities over several S cm$^{-1}$ have been also realized in several single component bis(dithiolene)-type metal complexes[25–27] ($\sigma_{RT}$ = 750 S cm$^{-1}$ at most[27], measured for single crystal). Highly conductive single component neutral radicals are also reported on several TTF derivatives having neutral radical units, such as nitronyl nitroxide[28] ($\sigma_{RT}$ = $9 \times 10^{-4}$ S cm$^{-1}$, measured for single crystal) and triphenylmethyl[29–31] ($\sigma_{RT}$ = $4 \times 10^{-1}$ S cm$^{-1}$ at most[29], measured for single crystal under 15.2 GPa).

Phenalenyl (**PNL**), a neutral π-radical based on polycyclic aromatic hydrocarbons, possesses a delocalized charge and electronic spin structure around the π-system[4,32–34]. Our recent studies on **PNL**-based π-radicals disclosed their intriguing electronic and dynamic functions originating from self-assembling ability by the π-stacks through intermolecular overlap of SOMO[33,34]. **PNL**-based radicals are also regarded as potential candidates of organic conductors, and high conductivities of zwitterionic bis**PNL** boron complexes[35–42] ($\sigma_{RT}$ = 0.3 S cm$^{-1}$ at most[38,39], measured for single crystal) and bis**PNL** singlet-biradicals[43] ($\sigma_{RT}$ = $5.0 \times 10^{-5}$ S cm$^{-1}$, measured for single crystals) have been disclosed. Conductivities of monomeric **PNL** neutral radicals have been also investigated, however, they were insulators as seen in 1,9-dithio**PNL**[44] ($\sigma_{RT}$ < ~$10^{-6}$ S cm$^{-1}$, measured for compressed pellets), perchloro**PNL**[45] ($\sigma_{RT}$ = $10^{-10}$ S cm$^{-1}$, measured for single crystals) and 2,5,8-tris(pentafluorophenyl)**PNL**[46] ($\sigma_{RT}$ < $1 \times 10^{-10}$ S cm$^{-1}$, measured for compressed pellets).

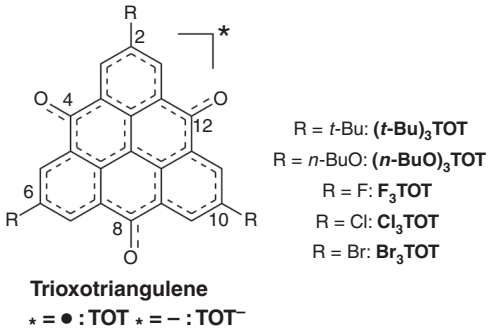


**Fig. 1** Molecular structure of **TOT**. **R** shows substituent groups, and the asterisk (*) represents the electronic states of the **TOT** skeleton

4,8,12-Trioxotriangulene (**TOT**, Fig. 1) can be designed by the 2D π-expansion and oxygen-atom substitution of **PNL** while retaining a three-fold molecular symmetry, and this carbon-centered neutral radical exhibits a peculiarly high stability even without steric protection due to the delocalization of electronic spin around the 25π-electronic system[47–50]. Our previous study on **TOT** derivatives having various substituent groups at the 2,6,10-positions (**R$_3$TOT**, respectively, Fig. 1) disclosed the self-assembling ability based on two-electron-multicenter bonding forming 1D π-stacking columns (π-stacked radical polymers)[47–49]. The strong intermolecular orbital overlap within the column demonstrated the near-infrared photo-absorption[48] and the high mobility *n*-type FET performance[51].

We propose that the 1D self-assembling ability and the large 25π-electronic system with a robust condensed polycyclic structure of **TOT** may also provide high electrical conductivities in the solid state. More importantly, these peculiar electronic and structural properties may give a unique chance to synthesize MV salts by formal charge injection into the 1D stacks of **TOT** neutral radical crystals. Here we report high electrical conductivities of **TOT** neutral radicals ($\sigma_{RT}$ = $10^{-4}$–$10^{-3}$ S cm$^{-1}$, measured for single crystals) as a single component purely organic molecular system, and a general tendency to form MV salts composed of neutral radicals and the corresponding anion species with further higher conductivities of $\sigma_{RT}$ = 1–125 S cm$^{-1}$.

## Results

**Stacking patterns and conductivities of TOT neutral radicals**. Figures 2 and 3 illustrates the π-stacking columns of **R$_3$TOT** derivatives (R = *t*-Bu, *n*-BuO, F, Br) and π-stacking patterns in the crystal structures, where the π-stacking patterns are modified with the aid of substituent effect[47,48]. The theoretical calculation on **(*t*-Bu)$_3$TOT** and **Br$_3$TOT** performed by Kinoshita et al. suggested that the electrical conductivity of π-stacking columns of **TOT** would be influenced by the stacking patterns within the 1D columns[52].

The π-stacking column of **(*t*-Bu)$_3$TOT** is formed by the 1D alignment of π-dimers with a staggered stacking pattern (Figs. 2a

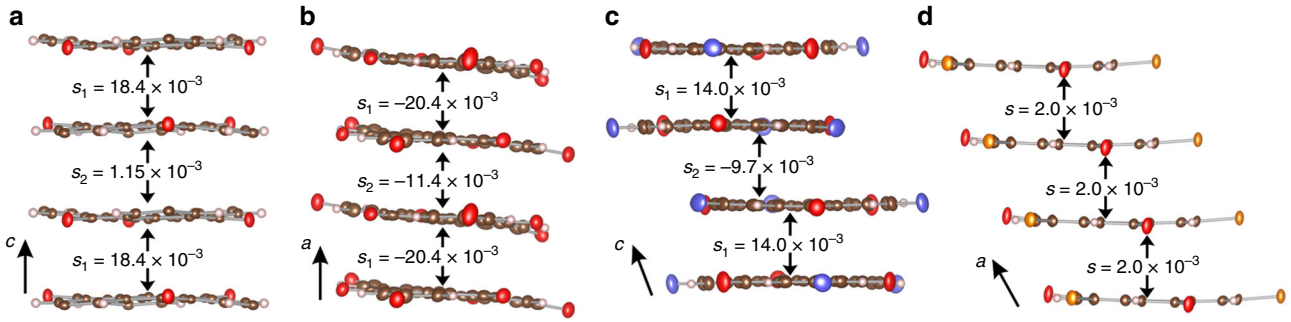


**Fig. 2** 1D π-stacked radical polymers of **TOT**. **a (*t*-Bu)$_3$TOT**, **b (*n*-BuO)$_3$TOT**, **c F$_3$TOT**, **d Br$_3$TOT**. Labels $s_1$ and $s_2$ are the intradimer and interdimer overlap integrals, respectively. In **a** and **b**, the butyl groups are omitted for clarity

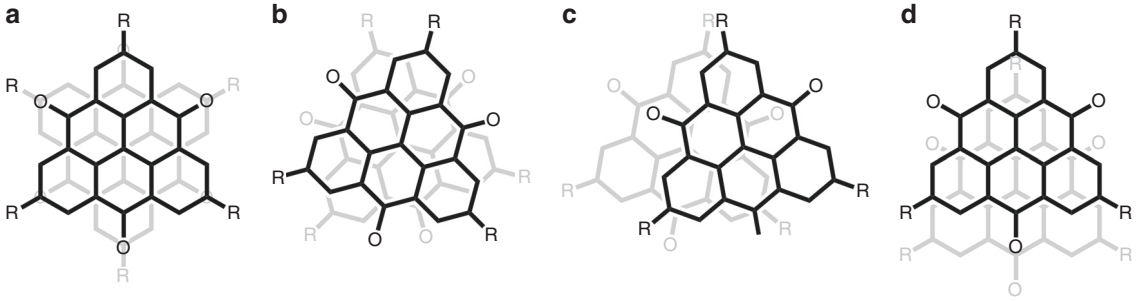


**Fig. 3** Stacking modes in π-stacking columns of **TOT** derivatives. **a** Staggered stack, **b** twisted stack, **c** fan-shaped stack, and **d** slipped stack

and 3a)[47,48], where intermolecular overlap integral within the π-dimer ($s_1$) was ~15 times larger than that of interdimer one ($s_2$) ($s_1/s_2 = 18.4 \times 10^{-3}/1.15 \times 10^{-3}$), indicating that a strong spin–spin coupling within the π-dimer reduces the carrier concentration and also cut off the conduction pathway. In the tight-binding band calculation based on the crystal structure, the energy dispersion of SOMOs is large along the stacking direction (Fig. 4a and Supplementary Figure 1a) due to significant face-to-face π–π interactions. The strong π-dimerization in the 1D column causes a large band splitting of 0.30 eV between upper and lower bands with narrow bandwidths of ~0.06 eV, showing the characteristics of a typical band insulator of **(*t*-Bu)$_3$TOT** ($\sigma_{RT}$ < $10^{-8}$ S cm$^{-1}$//*c*-axis). The insulating behavior of **(*t*-Bu)$_3$TOT** due to strong π-dimerization can be also seen in the solid state electronic spectrum, where the $\lambda_{max}$ of intermolecular transition was observed at 8800 cm$^{-1}$ (Fig. 5)[49]. In the case of **(*n*-BuO)$_3$TOT**, a weakly dimerized π-stacking column was formed, where the **TOT** skeleton stacked with twisting of ~32° and overlapping central carbon atoms (Figs. 2b and 3b). The interdimer overlap integral $s_2$ ($-11.4 \times 10^{-3}$) was much larger than that in **(*t*-Bu)$_3$TOT** (Fig. 2b), causing the larger band dispersion and a smaller band gap of 0.16 eV in **(*n*-BuO)$_3$TOT** (Fig. 4b). Such situation well coincides with the lower energy intermolecular transition, $\lambda_{max}$ = 6700 cm$^{-1}$ in the solid-state electronic spectrum (Fig. 5)[48], suggesting the higher concentration of carrier than that of **(*t*-Bu)$_3$TOT**. **(*n*-BuO)$_3$TOT** showed a high conductivity of $\sigma_{RT} = 1.2 \times 10^{-3}$ and a semiconducting behavior with an activation energy ($E_a$) = 296 meV (Fig. 6). In the π-stacking column of **F$_3$TOT**, the staggered π-dimer stacked with a fan-shaped stacking, where the central carbon atoms possessing the largest spin density did not overlap each other (Figs. 2c, 3a, and 3c). The interdimer interaction $s_2 = -9.7 \times 10^{-3}$ S cm$^{-1}$ was slightly smaller than that of **(*n*-BuO)$_3$TOT**. Due to the difference in the interdimer interaction, the band dispersion of **F$_3$TOT** became smaller than that of **(*n*-BuO)$_3$TOT** (Fig. 4c), resulting in

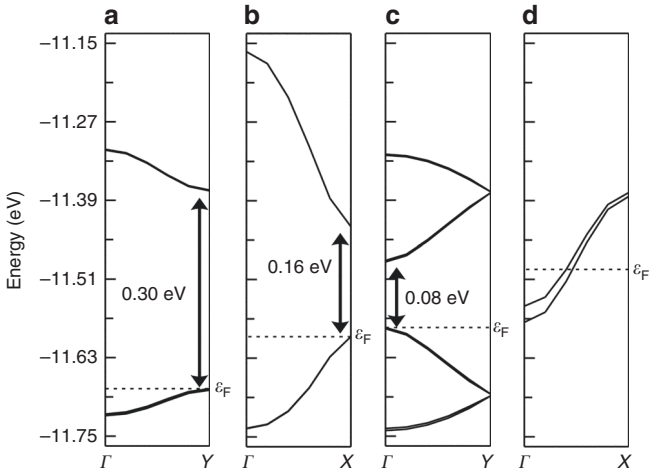


**Fig. 4** Band dispersions of SOMOs calculated for 1D columns of **TOT**. **a (*t*-Bu)$_3$TOT**, **b (*n*-BuO)$_3$TOT**, **c F$_3$TOT**, and **d Br$_3$TOT** (Γ = 0, 0, 0; *X* = 1/2, 0, 0; *Y* = 0, 0, 1/2, where the coordinates are given in units of the reciprocal lattice vectors)

the slightly lower conductivity of $\sigma_{RT} = 8.1 \times 10^{-5}$ S cm$^{-1}$ with $E_a$ = 304 meV (Fig. 6).

**Br$_3$TOT** forms a uniform π-stacking column with a large face-to-face distance of 3.43 Å and a slip-stacked pattern in the crystal structure (Figs. 2d and 3d)[47]. The overlap integral of SOMO within the column ($s = 2.0 \times 10^{-3}$) was ~$10^3$ times larger than those of intercolumnar directions. The band calculation gave a half-filled band with a bandwidth of 0.20 eV along the *a*-axis and a 1D Fermi surface (Fig. 4d and Supplementary Figure 1d). The electrical conductivity of the **Br$_3$TOT** single crystal measured along the stacking direction (*a*-axis) was $\sigma_{RT} = 1.8 \times 10^{-3}$ S cm$^{-1}$. The resistivity became larger with lowering temperature

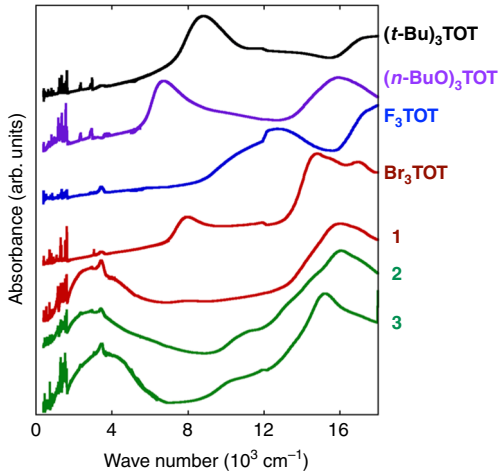


**Fig. 5** Electronic spectra of **TOT** derivatives and MV salts in KBr pellets. Low-energy absorption bands around 3000 $cm^{-1}$ in MV salts indicate the co-existence of neutral radical and monoanion species within the 1D column

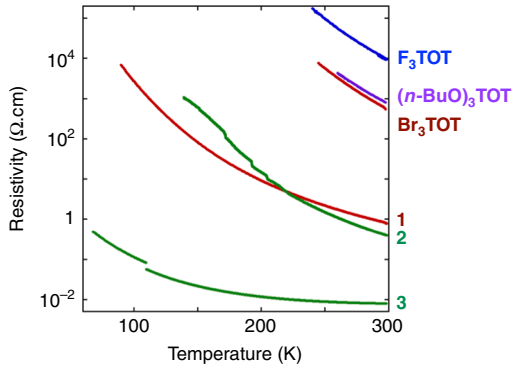


**Fig. 6** Temperature dependences of resistivities of **TOT** derivatives and MV salts. Measurement were performed for single crystals (//π-stacking direction). MV salts showed much lower resistivities than those of **TOT** neutral radicals

indicating the semiconducting nature with $E_a = 308$ meV (Fig. 6). These solid-state properties of **$Br_3$TOT** are well explained as a Mott-type insulator. It should be noted that the $\sigma_{RT}$ values of **(*n*-BuO)$_3$TOT** and **$Br_3$TOT** are very high as single component neutral radicals.

The high conductivity of **$Br_3$TOT** is achieved by the stable uniform π-stacked radical array forming conduction pathway. For the reduction of *U*, conduction barrier, extensive π-electronic system with the delocalization of charge and electronic spin is also essential. *U* of **TOT** derivatives can be experimentally evaluated by the difference between oxidation and reduction potentials in the electrochemical measurement. That value of **(*t*-Bu)$_3$TOT** in dichloromethane is 1.10 V (Supplementary Figure 3), and is much smaller than **PNL** radical (1.52 V)[53] and 2,2,6,6-tetramethylpiperidine-1-oxyl (TEMPO) radical (2.3 V, measured in our laboratory). The strong CT interaction within the column and reduction of *U* in **$Br_3$TOT** is also indicated by a low-energy absorption around 8000 $cm^{-1}$ in the solid-state electronic spectrum (Fig. 5) that can be assigned as an intermolecular CT band[48,54].

The intermolecular overlap integral in the **$Br_3$TOT** column was one order smaller than those of other derivatives, because the central carbon atoms having the largest SOMO coefficient were not close in the slipped stack (Fig. 3d). Due to the small overlap integral within the column, the bandwidth of **$Br_3$TOT** was 0.20 eV, and smaller than those of **(*n*-BuO)$_3$TOT** and **$F_3$TOT** (Fig. 2b–d). Since the conduction barrier in a 1D array of neutral radicals is defined as $U_{eff}$–4*t*, where $U_{eff}$ and *t* are the effective on-site Coulomb repulsive energy and the transfer integral of SOMOs, respectively, the strong orbital overlap is essential for the improvement of conductivity. A uniform π-stacking manner by strong face-to-face interaction with the overlapping of central carbon atoms would be the most effective for further high conductivity in single component **TOT** neutral radicals.

**Crystal structures and conductivities of MV salts**. These findings strongly encouraged us to prepare MV salts of **TOT** by formally injecting excess electrons into the 1D stacks of **TOT** neutral radical crystals. As a result, our continuous synthetic efforts finally found out a general preparation method for MV salts of **TOT**s formulated as (*n*-$Bu_4N^+$)(**$Br_3TOT^-$**)(**$Br_3TOT$**)$_2$(THF)$_2$ **1**, (*n*-$Bu_4N^+$)(**$Cl_3TOT^-$**)(**$Cl_3TOT$**) **2**, and ($Li^+$)(**$Cl_3TOT^-$**)(**$Cl_3TOT$**)$_x$($H_2O$)$_y$ **3** were obtained by the electrocrystallization of **$R_3TOT^-$** salts in appropriate solvents (Supplementary Figure 2). In the case of **3**, the component ratios *x* and *y* cannot be determined due to the severe disorder of $Li^+$ and crystalline water molecules. The MV state of **1**–**3** can be also confirmed by the solid-state electronic spectra (Fig. 5), where intermolecular CT bands between monoanion and neutral radical species are observed around 3000 $cm^{-1}$[54]. These bands suggest the high carrier concentration and high conductivity by the injection of excess electron into the column of neutral radicals.

Figure 7a shows the 1D π-stacking column in the crystal structure of **1**. The column was surrounded by *n*-$Bu_4N^+$ and THF molecules, resulting in the 1D electronic structure. There were five crystallographically independent **$Br_3$TOT** molecules (labeled as A–E in Fig. 7a) having a three-fold symmetry, and the E molecule also possessed a two-fold axis on the molecular plane. These molecules were aligned in the order of D–C–B–A–E–A–B–C–D as a repeating unit. The face-to-face stacking distances varied from 3.21 to 3.35 Å (Supplementary Figure 4), and smaller than the sum of the van der Waals radii of two carbon atoms (3.40 Å)[55]. In each stack of **$Br_3$TOT** molecules, the central carbon atoms, which possessed the largest SOMO coefficient and spin distribution[49,50], were close to each other, causing strong orbital overlaps (Supplementary Figure 4). The charge-distribution in the column was discussed by the C–O bond lengths of the **TOT** skeleton. The C–O bond lengths of **$Br_3$TOT** neutral radical is 1.223 Å and slightly shorter than that in the anion salt (1.244 Å) (averaged values, Supplementary Table 1)[47]. The similar relationship can be also seen in the neutral radical and monoanion species of **(*t*-Bu)$_3$TOT** (1.229 vs. 1.245 Å, respectively, Supplementary Table 1)[47–49]. The slightly longer C–O bond lengths in monoanion species is caused by the large electronegativity of the oxygen atom, stabilizing the resonance structures having C–O single bond character, where the minus charge locates on the oxygen atom. Since the differences in C–O bond lengths between neutral radical and monoanion species were small in comparison with experimental errors, the precise estimation of charge on each molecule could not be done. However, the longer C–O bond lengths in C and E molecules (1.251(9) and 1.240(17) Å, respectively) than the others (1.211(9)–1.214(9) Å) suggest the charge-separated state within the column (Supplementary Table 1). Accordingly, the column is constructed by the alternation of neutral radical dimer and anionic species as shown in Fig. 5a. The dimerization of neutral radicals in the column was supported by the strong antiferromagnetic coupling observed in the temperature-variable ESR measurement ($2J/k_B = -694$ K) (Supplementary Figure 6a)[56]. The

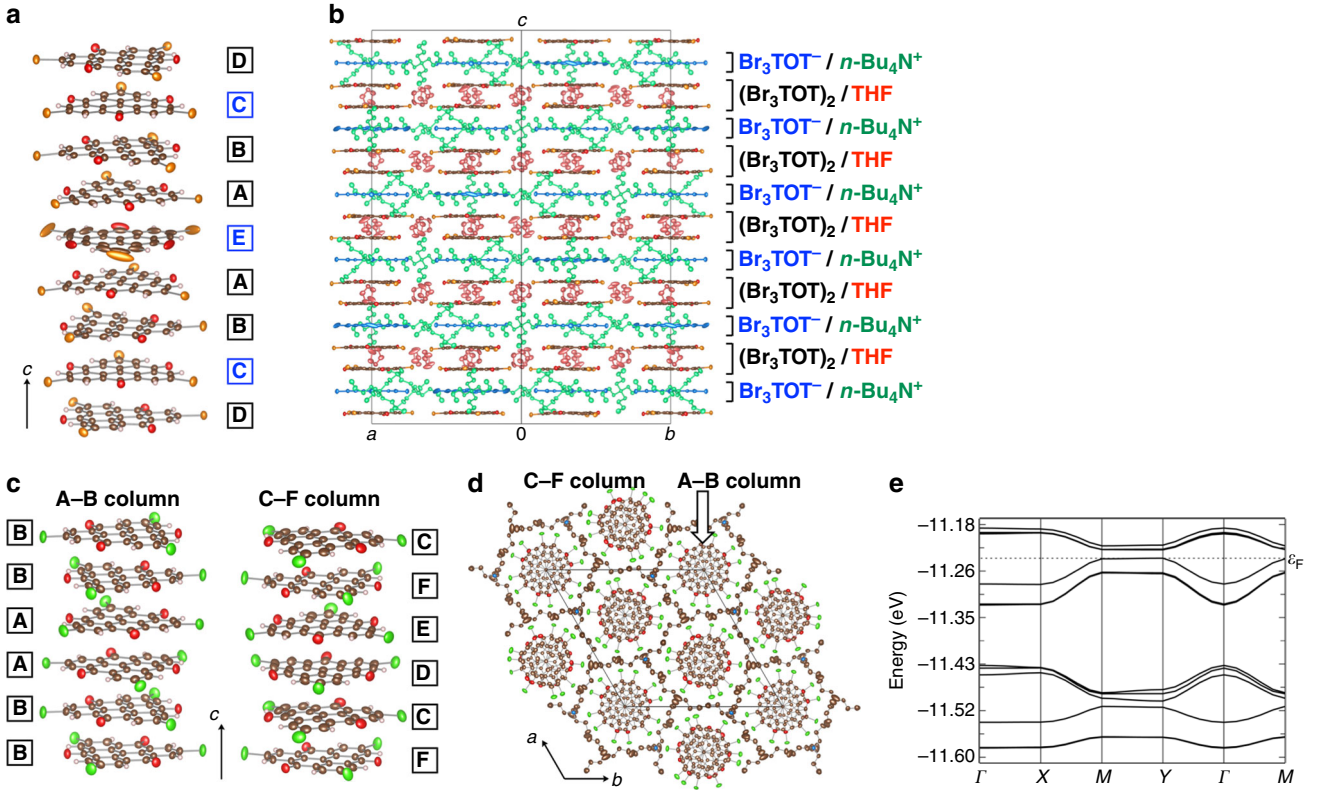


**Fig. 7** Crystal structures of MV salts **1** and **2**. **a** 1D π-stacked radical polymer of **1**. Molecules labeled as A–E are the crystallographically independent **$Br_3$TOT** molecules, and blue colored labels (C and E) present the anionic molecules. **b** Orientation of 1D columns. *n*-$Bu_4N^+$ and THF molecules on the [110] layer in **1** show anion–neutral radical layered structures. Green and red molecules are *n*-$Bu_4N^+$ and THF solvent, respectively. **c** 1D π-stacked radical polymer of **2**. Molecules labeled as A–F are the crystallographically independent **$Cl_3$TOT** molecules. **d** Crystal packing of **2** viewed along the *c*-axis. Hydrogen atom are omitted for clarity in **b** and **d**. **e** Calculated band structure of SOMO of **2** within the *ac*-plane based on the crystal structure at 290 K

anionic C and E molecules were arranged in a layered structure perpendicular to the stacking direction (blue molecules in Fig. 7b). The anion layer also included the *n*-$Bu_4N^+$ molecules (green molecules in Fig. 7b), indicating that the electrostatic interaction between the cation layer and **$Br_3$TOT** molecules induces the charge-separated state within the MV column. Due to the charge-separation and non-uniform overlap integrals (Supplementary Figure 4) in the column, **1** showed a semiconducting behavior with $E_a = 127$ meV (Fig. 6). The $\sigma_{RT}$ value, 1.3 S cm$^{-1}$, was three orders larger than that of **$Br_3$TOT** neutral radical crystal.

Similarly to **1**, the salt **2** was constructed by the 1D columns of **$Cl_3$TOT** molecules (A–B and C–F columns in Fig. 7c, d) that were surrounded by *n*-$Bu_4N^+$ molecules. The C–O bond lengths of each molecules varied in a range of 1.224(5)–1.240(4) Å (Supplementary Table 1), suggesting a charge-separated state also in these columns, although the distinct difference as seen in **1** was not found. The overlap integrals within both columns were not uniform (Supplementary Figure 5), causing the small band gap of ~0.02 meV of the SOMO band (Fig. 7e) at the Fermi level. The salt **2** exhibited a semiconducting behavior with $\sigma_{RT} = 2.5$ S cm$^{-1}$ and $E_a = 177$ meV (Fig. 6). The temperature dependence of the magnetic susceptibility showed a strong antiferromagnetic coupling within the columns (Supplementary Figure 6b, $2J/k_B = -1220$ K with the singlet–triplet model)[56].

The variation of counteraction highly affected the stacking pattern and the conductivity of the MV **TOT** columns, and the highest conductivity was obtained in the combination of $Li^+$ and **$Cl_3$TOT**. The crystal of **3** contained crystallographically independent two **$Cl_3$TOT** molecules (A and B) both of which possessed a three-fold symmetry. Molecules A and B individually formed 1D columns with the uniform stacking distance of 3.29 Å (A and B columns, Fig. 8a). The overlapping patterns were staggered (A, Fig. 8b) and twisted (B, Fig. 8c) modes, and the central carbons were close to each other, resulting in the strong orbital overlaps (overlap integrals of A and B columns: $s_A = 8.0 \times 10^{-3}$ and $s_B = 15.3 \times 10^{-3}$, respectively, Fig. 8a). The tight binding approximated calculation showed six SOMO/HOMO bands from six **$Cl_3$TOT** molecules in a unit cell, and indicated a 1D electronic structure along the stacking direction (Fig. 8d). The band dispersion of B column, 0.48 eV, was larger than that of A column (green and blue lines in Fig. 8d, respectively), reflecting the stronger orbital overlap within the B column. These calculations suggest that the B column can exhibit more effective charge-transport ability. The electrical conductivity of **3**, $\sigma_{RT} = 125$ S cm$^{-1}$, was two orders higher than those of *n*-$Bu_4N^+$ salts **1** and **2**, and the activation energy was 12 meV (Fig. 6). In the magnetic measurement, **3** showed a superimposition of two kinds of 1D antifferomagnetic chains of Bleaney–Bowers[56] and Bonner–Fisher[57] models (Supplementary Figure 7), suggesting that A and B columns exhibited different magnetic and conducting behaviors. The origin of the semiconducting behavior has not been clarified, however, the electrostatic perturbation due to $Li^+$ and $H_2O$ molecules might cause the conduction barrier (Fig. 8e). The temperature dependence of ESR intensity of **3** did not show any abrupt change due to phase transition even under the low temperature of ~4 K.

## Discussion

In conclusion, we have investigated electrical conductivities of π-stacked radical polymers of **TOT** derivatives. The extended

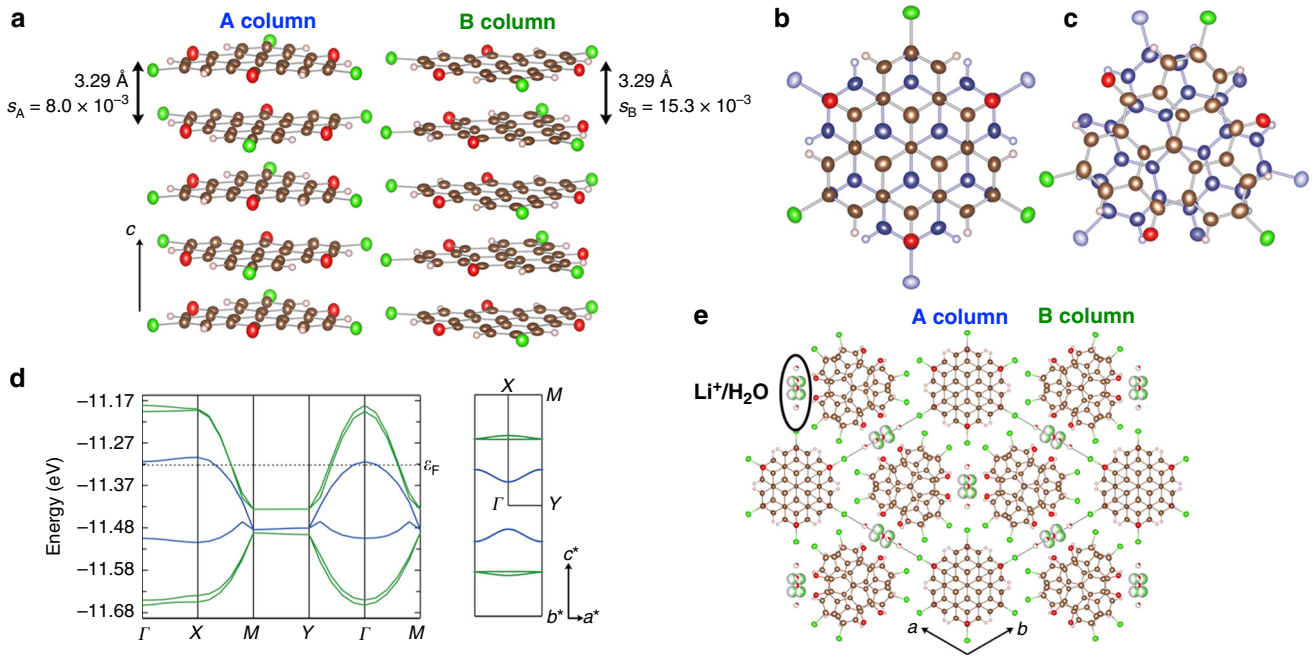


**Fig. 8** Crystal structure of salt **3**. **a** 1D π-stacked columns of **$Cl_3$TOT**. **b** and **c** Staggered and twisted overlapping pattern of molecules A and B, respectively. **d** Calculated band structure and Fermi surface within the *ac*-plane of SOMO of **3** based on the crystal structure at 100 K. Fermi energy ($\varepsilon_F$) and Fermi surface was calculated assuming the band filling of 0.75 ($x = 1$). Blue and green colored bands are formed by the A and B columns, respectively. **e** Crystal packing viewed along the *c*-axis, showing the arrangement of π-stacking columns and disordered $Li^+/H_2O$ molecules

π-electronic system with a charge-delocalization and strong π-stacks realized high conductivities of $\sigma_{RT} \sim 10^{-3}$ S cm$^{-1}$ as a single component, purely organic molecular system. The conductivity further increased in the MV salts, and the $Li^+$ salt **3** exhibited a notably high conductivity of $10^2$ S cm$^{-1}$ order, which is close to that of the TTF–TCNQ complex. Control of stacking patterns within the columns by diversifying counter cation and chemical modifications on the **TOT** skeleton will realize the further higher conductivity and metallic conduction in **TOT**-based π-stacked radical polymers. Furthermore, the application of high pressure to neutral radical and MV salts of **TOT** may dramatically increase the conductivity and realize a metallic behavior as reported in bisdithazolyl neutral radicals[13,15–17].

Material exploration for organic conductors revealed a number of intriguing functions and phenomena[1]. However, most previous studies are based on limited molecular skeletons, such as TTF, TCNQ, dithiolate-type complexes, $C_{60}$, etc. In the present study, **TOT** showed a general tendency to form 1D columns and MV salts exhibiting high conductivities. This result suggests the potential for **TOT** to serve as a molecular building block of organic conductors, and may provide a new milestone in the material exploration in the development of organic electronic materials. It should be noted that various chemical modifications on **TOT** skeleton, such as introduction of various substituent groups at R positions (Fig. 1) and oxo-groups[58,59], can be carried out, giving a chance to discover new phenomena and functions. Our current interest is aimed to the development of multifunctional organic conductors by the introduction of chirality[60,61] and coordination to metal ions.

## Methods

**Materials**. **TOT** derivatives and the monoanion salts were synthesized according to our previous papers[47–49]. Tetrabutylammonium tetrafluoroborate (($n$-$Bu_4N^+$)($BF_4^-$)) was purified by the recrystallization from ethanol. Solvents were dried (drying reagent in parenthesis) and distilled under an argon atmosphere prior to use: THF (Na–benzophenone ketyl); acetonitrile ($P_2O_5$/$CaH_2$); and methanol (Mg).

**Measurements**. Electronic spectra were measured for KBr pellets or solutions on a Shimadzu UV/vis scanning spectrophotometer UV-3100PC. Infrared spectrum was recorded on a JASCO FT/IR-660 Plus spectrometer on a KBr plate (resolution 2 cm$^{-1}$). Cyclic voltammetric measurement was made with an ALS Electrochemical Analyzer model 630A. Cyclic voltammogram was recorded with 3-mm-diameter carbon plate and Pt wire counter electrodes in dry $CH_2Cl_2$ containing 0.1 M $n$-$Bu_4NClO_4$ as supporting electrolyte at room temperature. The experiment employed a Ag/$AgNO_3$ reference electrode, and the final result was calibrated with ferrocene/ferrocenium couple. The magnetic properties were measured on a single crystal through an ESR Spectrometer Bruker E500 in the temperature range of 4–300 K. The DC magnetic susceptibility was measured at a field of 0.3 or 4.0 T with an MPMS-XL Quantum Design SQUID magnetometer in a temperature range of 2–350 K in an atmosphere of helium. DC conductivities were measured by a standard four-probe technique using gold wires of 10 μm diameter using carbon paste.

**X-ray crystallography**. X-ray crystallographic measurements were made on a Rigaku Raxis-Rapid imaging plate with graphite monochromated Mo Kα ($\lambda$ = 0.71075 Å). Structures were determined by a direct method using SIR2004[62]. Refinements were performed by a full-matrix least-squares on $F^2$ using the SHELXL-97[63]. All non-hydrogen atoms were refined anisotropically, and all hydrogen atoms were included but not refined. Empirical absorption corrections were applied. Selected crystal data collection parameters are given in Supplementary Table 2.

**Preparation of ($n$-$Bu_4N^+$)($Br_3TOT^-$)($Br_3TOT$)$_2$($THF$)$_2$ (salt 1)**. In an H-shaped cell with a glass frit separating two chambers, ($n$-$Bu_4N^+$)(**$Br_3TOT^-$**) (7.5 mg, 0.01 mmol) and ($n$-$Bu_4N^+$)($BF_4^-$) (33.5 mg, 0.10 mmol) were placed in the anodic and both chambers, respectively. After dissolving the salt and supporting electrolyte in THF (18 mL) under Ar atmosphere, a constant current of 1 μA was applied for 10 days between the platinum electrodes of the 1 mm diameter, yielding salt 1 (3.8 mg) as black needle crystals. Due to the efflorescence of the salt, elemental analysis could not be performed. In the measurements of ESR and electrical conductivity, the samples were coated with epoxy resin to prevent from decomposition of the crystals. The X-ray diffraction measurement was performed for a sample soaked in mineral oil and then frozen with a cold $N_2$ gas (200 K).

**Preparation of ($n$-$Bu_4N^+$)($Cl_3TOT^-$)($Cl_3TOT$) (2)**. In an H-shaped cell with a glass frit separating two chambers, ($n$-$Bu_4N^+$)(**$Cl_3TOT^-$**) (3.4 mg, 0.005 mmol) and ($n$-$Bu_4N^+$)($BF_4^-$) (34.6 mg, 0.10 mmol) were placed in the anodic and both chambers, respectively. After dissolving the donor and supporting electrolyte in acetonitrile (18 mL) under Ar atmosphere, a constant current of 0.5 μA was applied for 5 days between the platinum electrodes of the 1 mm diameter, yielding salt 2 (1.5 mg) as black needle crystals.

**Preparation of $(Li^+)(Cl_3TOT^-)(Cl_3TOT)_x(H_2O)_y$ (3)**. In an H-shaped cell with a glass frit separating two chambers, $(Li^+)(Cl_3TOT^-)$ (9.5 mg, 0.022 mmol) and $LiClO_4$ (83.3 mg, 0.78 mmol) were placed in the anodic and both chambers, respectively. After dissolving the salt and supporting electrolyte in methanol (18 mL) under Ar atmosphere, a constant current of 1.0 μA was applied for 14 days between the platinum electrodes of the 1 mm diameter, yielding salt 3 (1.2 mg) as black needle crystals.

**Data availability**. The X-ray crystallographic coordinates for the structures of MV salts **1**–**3** are available as Supplementary Data 1–3, respectively. These data have also been deposited at Cambridge Crystallographic Data Centre (CCDC), under deposition numbers CCDC1856410, CCDC1856411, and CCDC1856412. These data can be obtained free of charge from the CCDC via http://www.ccdc.cam.ac.uk/data_request/cif. The other data that support the findings of this study are available from the corresponding author upon reasonable request.

Received: 29 May 2018 Accepted: 26 July 2018
Published online: 30 August 2018

## References

1. Batail, P. Introduction: molecular conductors. *Chem. Rev.* **104**, 4887–4890 (2004).
2. Akamatu, H., Inokuchi, H. & Matsunaga, Y. Electrical conductivity of the perylene-bromine complex. *Nature* **173**, 168–169 (1954).
3. Ferraris, J., Cowan, D. O., Walatka, V. & Perlstein, J. H. Electron transfer in a new highly conducting donor-acceptor complex. *J. Am. Chem. Soc.* **95**, 948–945 (1973).
4. Haddon, R. C. Design of organic metals and superconductors. *Nature* **256**, 394–396 (1975).
5. Haddon, R. C. Quantum chemical studies in the design of organic metals. II. The equilibrium geometries and electronic structure of tetrathiofulvalene (ttf) and tetracyanoquinodimethane (tcnq) and their uni- and di-valent ions. *Aust. J. Chem.* **28**, 2333–2342 (1975).
6. Haddon, R. C. Metals and superconductors: molecular analogs of atomic hydrogen. *Chemphyschem* **13**, 3581–3583 (2012).
7. Torrance, J. B. The Difference between metallic and insulating salts of tetracyanoquinodimethane (TCNQ): how to design an organic metal. *Acc. Chem. Res.* **12**, 79–86 (1979).
8. Garito, A. F. & Heeger, A. J. The design and synthesis of organic metals. *Acc. Chem. Res.* **7**, 232–240 (1974).
9. Eley, D. D., Jones, K. W., Littler, J. G. F. & Willis, M. R. Semiconductivity of organic substances. Part 10. Electrical properties of galvinoxyl, *α,α*-diphenyl-*β*-picryl hydrazyl and related solid free radicals. *Trans. Faraday Soc.* **62**, 3192–3200 (1966).
10. Inokuchi, H., Harada, Y. & Maruyama, Y. Electric properties of the single-crystal and thin film of *α,α′*-diphenyl-*β*-picrylhydrazyl. *Bull. Chem. Soc. Jpn.* **35**, 1559–1561 (1962).
11. Hicks, R. G. The Synthesis and characterization of stable radicals containing the thiazyl (SN) fragment and their use as building blocks for advanced functional materials. In *Stable Radicals: Fundamentals and Applied Aspects of Odd-electron Compounds* (ed. Hicks, R. G.) 317−380 (John Wiley & Sons, Chichester, 2010).
12. Yu, X. et al. Semiquinone-bridged bisdithiazolyl radicals as neutral radical conductors. *J. Am. Chem. Soc.* **134**, 2264–2275 (2012).
13. Mailman, A. et al. Crossing the insulator-to-metal barrier with a thiazyl radical conductor. *J. Am. Chem. Soc.* **134**, 9886–9889 (2012).
14. Wong, J. W. L. et al. Supramolecular architecture, crystal structure and transport properties of the prototypal oxobenzene-bridged bisdithiazolyl radical conductor. *Chem. Commun.* **50**, 785–787 (2014).
15. Wong, J. W. L. et al. Pressure induced phase transitions and metallization of a neutral radical conductor. *J. Am. Chem. Soc.* **136**, 1070–1081 (2014).
16. Tian, D. et al. The metallic state in neutral radical conductors: dimensionality, pressure and multiple orbital effects. *J. Am. Chem. Soc.* **137**, 14136–14148 (2015).
17. Mailman, A. et al. Fine tuning the performance of multiorbital radical conductors by substituent effects. *J. Am. Chem. Soc.* **139**, 1625–1635 (2017).
18. Tsubata, Y., Suzuki, T. & Miyashi, T. Single-component organic conductors based on neutral radicals containing the pyrazino-TCNQ skeleton. *J. Org. Chem.* **57**, 6749–6755 (1992).
19. Suzuki, T., Yamashita, Y., Imaeda, K., Ishida, T. & Nogami, T. Single-component organic semiconductors based on novel radicals that exhibit electrochemical amphotericity: preparation, crystal structures, and solid-state properties of *N,N*′-dicyanopyrazinonaphthoquinodiiminides substituted with an *N*-alkylpyridinium unit. *J. Org. Chem.* **66**, 216–224 (2001).
20. Neilands, O. Dioxo-and aminooxopyrimido-fused tetrathiafulvalenes-base compounds for novel organic semiconductors and for design of sensors for recognition of nucleic acid components. *Mol. Cryst. Liq. Cryst.* **335**, 331–349 (2001).
21. Bryan, C. D. et al. Conducting charge-transfer salts based on neutral π-radicals. *Nature* **365**, 821–823 (1993).
22. Awaga, K. et al. Multi-dimensional crystal structures and unique solid-state properties of heterocyclic thiazyl radicals and related materials. *Bull. Chem. Soc. Jpn.* **79**, 25–34 (2006).
23. Kobayashi, Y., Terauchi, T., Sumi, S. & Matsushita, Y. Carrier generation and electronic properties of a single-component pure organic metal. *Nat. Mater.* **16**, 109–115 (2017).
24. Tanaka, H., Okano, H., Kobayashi, H., Suzuki, W. & Kobayashi, A. A three-dimensional synthetic metallic crystal composed of single-component molecules. *Science* **291**, 285–287 (2001).
25. Belo, D. et al. Gold complexes with dithiothiophene ligands: a metal based on a neutral molecule. *Chem. Eur. J.* **7**, 511–519 (2001).
26. Filatre-Furcate, A. et al. Single-component conductors: a study electronic structure generated by bulky substituents. *Inorg. Chem.* **55**, 6036–6046 (2016).
27. Gal, Y. L. et al. Stable metallic state of a neutral-radical single-component conductor at ambient pressure. *J. Am. Chem. Soc.* **140**, 6998–7004 (2018).
28. Komatsu, H. et al. Influence of magnetic field upon the conductance of a unicomponent crystal of a tetrathiafulvalene-based nitronyl nitroxide. *J. Am. Chem. Soc.* **132**, 4528–4529 (2010).
29. Souto, M. et al. Pressure-induced conductivity in a neutral nonplanar spin-localized radical. *J. Am. Chem. Soc.* **138**, 11517–11525 (2016).
30. Souto, M., Rovira, C., Ratera, I. & Veciana, J. TTF–PTM dyads: from switched molecular self assembly in solution to radical conductors in solid state. *CrystEngComm* **19**, 197–206 (2017).
31. Souto, M. et al. Role of the open-shell character on the pressure-induced conductivity of an organic donor–acceptor radical dyad. *Chem. Eur. J.* **24**, 5500–5505 (2018).
32. Reid, D. H. The chemistry of the phenalenes. *Q. Rev.* **19**, 274–302 (1965).
33. Morita, Y., Suzuki, S., Sato, K. & Takui, T. Synthetic organic spin chemistry for structurally well-defined open-shell graphene fragments. *Nat. Chem.* **3**, 197–204 (2011).
34. Morita, Y. & Nishida, S. Phenalenyls, cyclopentadienyls, and other carbon-centered radicals. In *Stable radicals: Fundamentals and Applied Aspects of Odd-electron Compounds* (ed. Hicks, R. G.), 81–145 (John Wiley & Sons, Chichester, 2010).
35. Chi, X. et al. The first phenalenyl-based neutral radical molecular conductor. *J. Am. Chem. Soc.* **121**, 10395–10402 (1999).
36. Chi, X. et al. Dimeric phenalenyl-based neutral radical molecular conductors. *J. Am. Chem. Soc.* **123**, 4041–4048 (2001).
37. Pal, S. K. et al. Synthesis, structure and physical properties of the first one-dimensional phenalenyl-based neutral radical molecular conductor. *J. Am. Chem. Soc.* **126**, 1478–1484 (2004).
38. Pal, S. K. et al. Resonating valence-bond ground state in a phenalenyl-based neutral radical conductor. *Science* **309**, 281–284 (2005).
39. Mandal, S. K. et al. Resonating valence bond ground state in oxygen-functionalized phenalenyl-based neutral radical molecular conductors. *J. Am. Chem. Soc.* **128**, 1982–1994 (2006).
40. Bag, P. et al. Resonating valence bond and σ-charge density wave phases in a benzannulated phenalenyl radical. *J. Am. Chem. Soc.* **132**, 2684–2694 (2010).
41. Sarkar, A. et al. Synthesis, structure, and physical properties of a partial π-stacked phenalenyl-based neutral radical molecular conductor. *Chem. Eur. J.* **17**, 11576–11584 (2011).
42. Sarkar, A. et al. Sulfur and selenium substituted spiro-biphenalenyl-boron neutral radicals. *J. Mater. Chem.* **22**, 8245–8256 (2012).
43. Kubo, T. et al. Synthesis, intermolecular interaction, and semiconductive behavior of a delocalized singlet biradical hydrocarbon. *Angew. Chem. Int. Ed.* **44**, 6564–6568 (2005).
44. Beer, L. et al. The first electronically stabilized phenalenyl radical: effect of substituents on solution chemistry and solid-state structure. *Cryst. Growth Des.* **7**, 802–809 (2007).
45. Koutentis, P. A. et al. Perchlorophenalenyl radical. *J. Am. Chem. Soc.* **123**, 3864–3871 (2001).
46. Uchida, K. et al. Dual association modes of the 2,5,8-tris(pentafluorophenyl) phenalenyl radical. *Chem. Asian J.* **9**, 1823–1829 (2014).
47. Morita, Y. et al. Organic tailored batteries materials using stable open-shell molecules with degenerate frontier orbitals. *Nat. Mater.* **10**, 947–951 (2011).
48. Ikabata, Y. et al. Near-infrared absorption of π-stacking columns composed of trioxotriangulene neutral radicals. *npj Quantum Mater.* **2**, 27 (2017).
49. Morita, Y. et al. Trioxotriangulene: air- and thermally stable organic polycyclic carbon-centered neutral π-radical without steric protection. *Bull. Chem. Soc. Jpn.* **91**, 922–931 (2018).
50. Ikabata, Y., Akiba, K. & Nakai, H. Superphenalenyl: theoretical design of a π-conjugated planar hydrocarbon radical. *Chem. Lett.* **42**, 1386–1387 (2013).

51. Morita, Y. et al. Organic semiconductor material with neutral radical compound of a trioxotriangulene derivative as a semiconductor material. US Patent 8933437 B2 (2009).
52. Kinoshita, K. et al. Theoretical studies on the magnetic and conductive properties of crystals containing open-shell trioxotriangulene radicals. *Bull. Chem. Soc. Jpn.* **89**, 315–333 (2016).
53. Goto, K. et al. A stable neutral hydrocarbon radical: Synthesis, crystal structure, and physical properties of 2,5,8-tri-*tert*-butyl-phenalenyl. *J. Am. Chem. Soc.* **121**, 1619–1620 (1999).
54. Torrance, J. B., Scott, B. A., Welber, B., Kaufman, F. B. & Seiden, P. E. Optical properties of the radical cation tetrathiafulvalenium ($TTF^{+}$) in its mixed-valence and monovalence halide salts. *Phys. Rev. B* **19**, 730–741 (1979).
55. Bondi, A. van der Waals volumes and radii. *J. Phys. Chem.* **68**, 441–451 (1964).
56. Bleany, B. & Bowers, D. K. Anomalous paramagnetism of copper acetate. *Proc. R. Soc. Lond. Sec. A* **214**, 451–465 (1952).
57. Bonner, J. C. & Fisher, M. E. Linear magnetic chains with anisotropic coupling. *Phys. Rev.* **135**, A640–A658 (1964).
58. Ueda, A. et al. An extremely redox-active air-stable neutral π radical: dicyanomethylene-substituted triangulene with a threefold symmetry. *Chem. Eur. J.* **18**, 16272–16276 (2012).
59. Ueda, A. et al. A dicyanomethylene-substituted triangulene: effects of molecular- symmetry reduction and electron-accepting substituents on a fused polycyclic neutral π-radical system. *Chem. Asian J.* **8**, 2057–2063 (2013).
60. Avarvari, N. & Wallis, J. D. Strategies towards chiral molecular conductors. *J. Mater. Chem.* **19**, 4061–4076 (2009).
61. Pop, F., Auban-Senzier, P., Canadell, F., Rikken, G. L. J. A. & Avarvari, N. Electrical magnetochiral anisotropy in a bulk chiral molecular conductor. *Nat. Commun.* **5**, 4757 (2014).
62. Burla, M. C. et al. SIR2004: an improved tool for crystal structure determination and refinement. *J. Appl. Crystallogr.* **38**, 381–388 (2005).
63. Sheldrick, G. M. A short history of SHELX. *Acta Crystallogr. Sect. A* **64**, 112–122 (2008).


## Acknowledgements

We thank Dr. M. Ishikawa and Prof. H. Yamochi, Kyoto University for their technical assistances in the electrical conductivity measurements. This work was supported by the Canon Foundation, the Grants-in-Aid for Scientific Research B (Nos. 25288022 and 16H04114) and Elements Science and Technology Project from the Ministry of Education, Culture, Sports, Science and Technology, Japan, and Core Research for Evolutional Science and Technology (CREST) Basic Research Program "Creation of Innovative Functions of Intelligent Materials on the Basis of Element Strategy" of Japan Science and Technology Agency (JST).

## Author contributions

Y.M. planned this project. T.M. and C.Y. prepared the materials and demonstrated spectroscopic analyses and measurement of transport properties. T.M. carried out X-ray crystal structure analyses and the tight-binding band calculation. K.F. measured ESR and magnetic susceptibilities of **1**–**3**. All authors wrote and reviewed the manuscript.

## Additional information

**Supplementary information** accompanies this paper at https://doi.org/10.1038/s42004-018-0048-5.

**Competing interests:** The authors declare no competing interests.

**Reprints and permission** information is available online at http://npg.nature.com/reprintsandpermissions/

**Publisher's note:** Springer Nature remains neutral with regard to jurisdictional claims in published maps and institutional affiliations.